A Molecular Thermometer for Nanoparticles for Optical Hyperthermia

12 AUTHORS, INCLUDING:

Laura D'Alfonso
Università degli Studi di Milano-Bicocca
57 PUBLICATIONS **716** CITATIONS

SEE PROFILE

Maddalena Collini
Università degli Studi di Milano-Bicocca
79 PUBLICATIONS **1,196** CITATIONS

SEE PROFILE

Giovanni Baldi
CE.RI.COL Colorobbia Research Centre
72 PUBLICATIONS **1,077** CITATIONS

SEE PROFILE

Daniela Maggioni
University of Milan
29 PUBLICATIONS **454** CITATIONS

SEE PROFILE

A Molecular Thermometer for Nanoparticles for Optical Hyperthermia

Stefano Freddi,[†] Laura Sironi,[†] Rocco D'Antuono,[†] Diego Morone,[†] Alice Donà,[‡] Elisa Cabrini,[‡] Laura D'Alfonso,[†] Maddalena Collini,[†] Piersandro Pallavicini,*[,‡] Giovanni Baldi,[§] Daniela Maggioni,[‖] and Giuseppe Chirico*[,†]

[†]Physics Department, Università degli Studi di Milano Bicocca, Piazza della Scienza 3, I-20126 Milano, Italy
[‡]Chemistry Department, Università degli Studi di Pavia, viale Taramelli 12, I-27100, Pavia, Italy
[§]Nanobiotechnology Department, Colorobbia Italia-Cericol, Via Pietramarina, 123, Sovigliana Vinci, Italy
[‖]Inorganic Chemistry Department, Università degli Studi di Milano, Via Venezian 21, 20133, Milano (I), Italy

S Supporting Information

ABSTRACT: We developed an all-optical method to measure the temperature on gold (nanorods and nanostars) and magnetite nanoparticles under near-infrared and radiofrequency excitation by monitoring the excited state lifetime of Rhodamine B that lies within ≅20 nm from the nanoparticle surface. We reached high temperature sensitivity (0.029 ± 0.001 ns/°C) and low uncertainty (±0.3 °C). Gold nanostars are ≅3 and ≅100 times more efficient than gold nanorods and magnetite nanoparticles in inducing localized hyperthermia.

KEYWORDS: Fluorescence, thermology, gold nanoparticles, near-infrared, hyperthermia
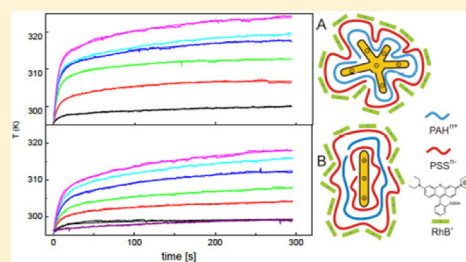
H yperthermia consists of killing tumor cells by heating them up at temperatures above 40 °C, and it has been already exploited at a preclinical level[1] also in combination with radiation therapy.[2,3] Radiofrequency or optically activated hyperthermia partially exploits the lower thermo-tolerance of cancer cells due to their reduced blood supply.[4] Limitations to the application of hyperthermia come instead from the observations that temperatures above 42 °C induce cell death also in healthy tissues marginal to tumors.[1,5] The possibility to damage the healthy tissues is therefore a real threat, and there is a clear need to enhance the hyperthermia efficiency and to measure the local temperature on the irradiated site. The thermal load is dramatically increased by employing gold nanorods[6,7] or paramagnetic iron-oxide nanoparticles.[1,8]

In nanoparticle-promoted hyperthermia, a direct temperature measurement has been obtained from thermal imaging,[6] that despite its sensitivity has a limited spatial resolution (10 μm) and is a surface measurement, and by nuclear magnetic resonance (NMR).[9,10] Recently a cyanine dye has been coupled to a quantum dot in a Förster resonance energy transfer (FRET) based device, used in HeLa and epithelial cells with a sensitivity ≅0.2 °C. However, the response of this probe changes in various environments, implying the need for a specific system calibration,[11] and the temperature probe relies on a nanoparticle different from the ones used for hyperthermia. Similar environmental sensitivity and calibration needs must be overcome with other molecule-based thermometers, which may in principle be used with hyperthermic nanoparticles: dyes displaying fluorescence[12] and phosphorescence

enhancement,[13] or Rhodamine B showing emission sensitivity (3.4% °C⁻¹) on temperature.[14] Intensive parameters are then to be sought: for example Donner et al.,[15] have devised a GFP based intracellular temperature probe based on the temperature dependence of the fluorescence polarization anisotropy. Also in this case, however, environmental dependences arise from local friction changes due to cytosol composition and protein adsorption. Very recently Okabe et al.[16] reported intracellular mapping of temperature by measuring the excited state lifetime of a water-sensitive metylacrylamide (DBD-AA) carried by a small (≅8−9 nm) fluorescent polymeric nanogel. The temperature resolution was ≅0.2−0.6 °C; the calibration was performed in extracts of COS7 cells, used for temperature mapping, and the results do not appear to depend on the probe concentration, proteins in the extracts, and medium viscosity.[16] Similar methods would then be interesting to measure the temperature around the irradiated nanoparticles independent of the type of radiation and nanoparticles, with reduced sensitivity to the chemical characteristics of the environment and without the need for a system-dependent calibration.

In this work we report an all-optical method to monitor the temperature increase in the close proximity of gold and magnetite nanoparticles that is also fairly independent of the specific environment used: a fluorophore is electrostatically bound and placed at a controlled nanometric distance from the
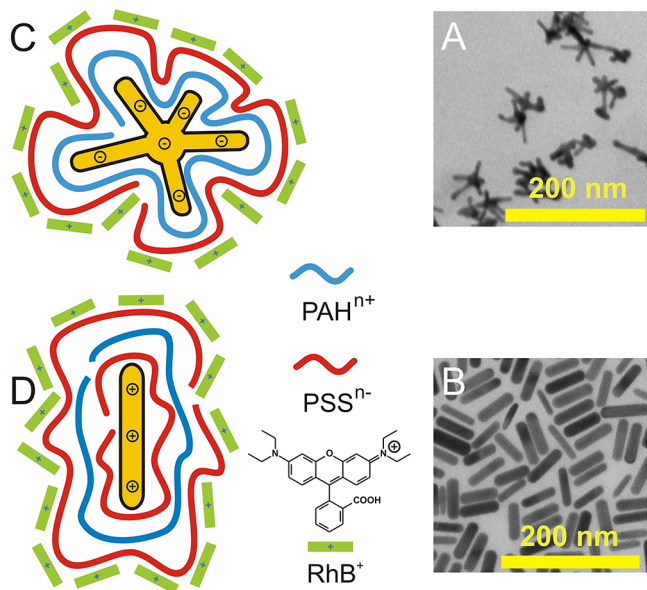
surface of the nanoparticles, allowing to monitor the local temperature through its excited state lifetime (ESL).

Paramagnetic nanoparticles and nonspherical gold nanoparticles are capable of inducing local thermal loads.[17] In this work we have used gold nanorods (GNRs)[18] that are endowed with near-infrared (NIR) resonances with large absorption and gold branched nanoparticles with reduced encumbrance, called here gold nanostars (GNSs), that we have recently synthesized, showing a high axial ratio;[19−21] see Scheme 1A and B. These nanoparticles display large NIR resonances that can be used to induce hyperthermia. As reference paramagnetic nanoloaders we take here magnetite nanoparticles.[22,23]

Scheme 1. Sample TEM images of the Nanostars (Panel A) and Nanorods (Panel B). Sketch of the Nanostars (Panel C) and Nanorods (Panel D) decorated with PSS (Red) and PAH (Light Blue) polymers and finally with RhB⁺ (Green and Chemical Structure)
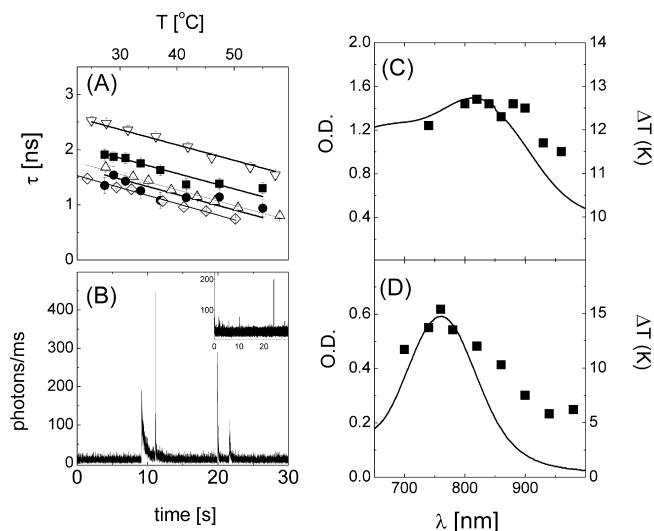
Figure 1. Panel A: Excited state lifetime (ESL) measured on RhB in water solutions (water pH = 5.84, △; PSS solution, ▽; water at pH = 2.2, ◇) and in suspensions of RhB decorated gold nanorods (ESL measured on fluorescence bursts, ●; ESL measured on the background, ■). The solid line corresponds to a slope $(d\tau/dT) = -(0.028 \pm 0.004)$ ns/°C, obtained from a global fit of all the data sets with different intercepts. Panel B: a fluorescence trace measured under tight laser focusing of a 20 nM suspension of nanoparticles decorated with two/three layers of polyelectrolytes and RhB. Four bursts are visible over a flat background. The inset reports a fluorescence trace acquired from a suspensions of gold nanorods decorated with a PAH and a PSS layers and incubated with RhB (then extensively washed out). Rare bursts are visible in this case. Panel C and D: optical density spectrum of gold nanorods (panel C, continuous line) and gold nanostars (panel D, continuous line). Full symbols represent the equilibrium temperature reached under continuous IR irradiation for 300 s (measured from thermograms). The suspensions ($C = 0.2$ mg/mL, gold nanorods, and $C = 0.25$ mg/mL for gold nanostars) were placed in plastic wells and irradiated by a collimated 1.2 mm (diameter) tunable NIR laser. Excitation intensity was $I_{exc} = 4.4$ W/cm².

Calibration of RhB for Temperature Measurements. Our choice for the reporter dye has fallen on Rhodamine B (RhB, see Scheme 1), whose ESL has a marked temperature dependence in aqueous solutions, $\partial\tau/\partial t \cong 0.029 \pm 0.001$ ns/°C.[24] It could be used as reliable temperature reporter if $\partial\tau/\partial t$ were slightly affected by surface−dye interactions. We studied the ESL temperature dependence of RhB when bound to gold nanorods, to our new GNSs)[19−21] and to paramagnetic Fe_3O_4 nanoparticles.

The bulk water calibration curve in the 10−60 °C range (Figure 1A, open up triangles) was obtained on water solutions of 2×10^{-6} M RhB, self-regulating at a 5.84 pH value:

$$\tau = [(2.4 \pm 0.3) - (0.029 \pm 0.005)T(°C)] \text{ ns} \qquad (1)$$

RhB exists in a positive (RhB⁺) and in a zwitterionic (RhB±) form, in equilibrium by the deprotonation of the −COOH function (Supporting Information, SI). The pK_a of the −COOH group strongly depends on the species present in solution: it has been reported to shift from 3.22 in water to 5.70 in 0.001 M sodium dodecylsulfate.[25] For sake of clarity, we measured the pK_a of RhB⁺ under our working conditions, finding 3.3 in water (SI). At pH 5.84 the molecule is thus ~100% RhB±. To be sure that the state of RhB does not

influence the τ vs T dependence, we repeated the calibration after acid addition, at pH 2.2 (100% RhB⁺), obtaining (Figure 1A, open diamonds) $\tau = [(2.2 \pm 0.03) - (0.029 \pm 0.001) T(°C)]$ ns.

The interaction of a dye with the metal surface in gold nanoparticles is well-known to reduce ESL by quenching.[26,27] To avoid this we have decorated the gold nanoparticles with alternate layers of positive (PAH) and negative (PSS) polyelectrolytes. Each polyelectrolyte layer adds 2.2 nm thickness to the nano-objects (when Cl⁻ ions are used).[28] A PSS-PAH-PSS triple layer was used for the positively charged GNRs and a PAH-PSS double layer for the negatively charged GNSs (see Scheme 1). The coating procedure terminated in all cases with a PSS layer, offering a negative surface for the adhesion of Rhodamine B in its cationic RhB⁺ form. We remeasured the pK_a of RhB in aqueous solution in the presence of PSS (SI), finding a predictable pK_a shift to 5.13, due to the electrostatic effect played by the negative charges in the polymer interacting with the acid function interaction.[29] After decoration of GNR with PSS/PAH/PSS and of GNS with PAH/PSS the measured pH is 5.37 and 4.33, granting in both cases a rich population of RhB⁺ in solution for further nanoparticle decoration by electrostatic interaction, as sketched in Scheme 1C and D. A direct demonstration of the polymer

coating and of the RhB[+] adsorption onto the nanoparticle surface came from the zeta potential (see Table S4) and from the observation that no or rare fluorescence bursts were observed from uncoated nanoparticle suspension (Figure 1B, inset).

Since PSS is used as negative outer polyelectrolyte layer to host the cationic dye, we have performed also a calibration curve of the temperature response of the RhB ESL when dissolved in PSS solutions. The measured pH under the experimental conditions was 5.89, corresponding to an equilibrium distribution of RhB[±] 84% and RhB[+] 16%. As observed in Figure 1A (down open triangles) the effect of the PSS polymer is to lengthen the ESL from the value measured in water, $\tau \cong 1.8$ ns at $T = 25$ °C, to a value of $\tau = 2.53 \pm 0.08$ ns at the same temperature. However the dependence of the RhB ESL on the bulk temperature is not markedly affected (Figure 1A).

The ESL of RhB[+] on nanoparticles as a function of the bulk temperature (controlled by a thermostatted bath, see Materials and Methods in SI) was measured on diluted suspensions of RhB[+] decorated nanoparticles under two-photon excitation at λ = 800 nm (80 MHz rep. rate; 250 fs pulse width, beam waist $\cong$ 0.8 μm, average power $\langle P \rangle \cong 2-4$ mW). In this case the fluorescence traces are characterized by bursts (Figure 1B) that correspond to the two-photon primed emission of a number of dyes adsorbed on the diffusing nanoparticles[27,30] on a flat background that is due to residual unbound dyes probably intermixed to PSS polymer. It is noteworthy that rare fluorescence bursts were detected from suspensions of nanoparticles decorated with PAH and incubated with RhB, similarly to what observed for undecorated nanoparticles (Figure 1B). This is a further clear indication that we are observing fluorescent RhB[+] molecules electrostatically bound to the negative surface of the nanoparticles. We verified that two polymeric layers were needed ($\cong$2.2 nm spacing per layer[28]) in order to avoid extensive quenching of the RhB fluorescence (Figure S11). Two exponential decays were detected in the ESL distribution: the shorter component is due to the gold nanoparticle intrinsic luminescence lifetime (relaxation time $\cong$ 0.3 ns)[20] under pulsed excitation at 800 nm, and the longer component was ascribed to the RhB[+] dyes that lie within a Debye length[31] from the outer PSS layer that covers the nanoparticle surface. The effect of gold on the RhB lifetime is remarkable, $\tau \cong 1.6$ ns at $T = 25$ °C (Figure 1A, full circles) to be compared to the value obtained in PSS solutions at similar temperatures (Figure 1A, open down triangles). Indeed, the gold nanoparticles have surface plasmon resonances also in the visible range ($\cong$520 nm)[19] that are superimposed on the RhB excitation spectrum and have therefore a large effect on the RhB excited state lifetime.

The relevant observation (Figure 1A) is however that in all of the cases investigated here (RhB solutions and RhB decorated GNSs suspensions) the temperature dependence of the RhB excited state lifetime is very similar and can therefore be used to characterize the system temperature. A global fit of all of the data sets reported in Figure 1A provides the slope ($d\tau/dT$) = $-(0.028 \pm 0.004)$ ns/°C, very close to the value measured for RhB in bulk water.[24] We can then apply this calibration to monitor the temperature close to the gold or magnetite nanoparticles under NIR or radiofrequency irradiation, respectively.
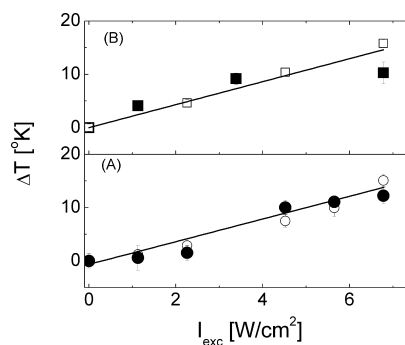
Temperature Increase from Irradiated Nanoparticles: Excited State Lifetime Measurements. A substantial thermal load in gold nanoparticles suspensions[32] and gold nanoparticle treated tissues[17] arises from the relevant absorption cross-section for NIR radiation of these nanoparticles.[6,33,34] Gold nanorods have two plasmonic modes that appear as well-defined resonances in the extinction spectrum at $\cong$ 520 nm and in NIR region at 760 nm (Figure 1C, the higher energy resonance at 520 nm is not shown here). Gold nanostars instead show a more complex extinction spectrum (Figure 1D). These nanoparticles occur in two populations[19,21] characterized by different axial ratio of branches and extinction spectra, but under the synthetic conditions used for their synthesis in the present paper, they are >70% in the form of pentatwinned stars,[21] displaying two wide bands,[20,21] the less energetic one corresponding to the most relevant absorption component[19,33] and placed at ~800 nm.

We irradiated suspensions of decorated nanoparticles (CW laser at λ = 800 nm, irradiation area 2 mm, intensity $\cong$ 4 W/cm^{2}, see SI) while measuring the RhB ESL (two-photon excitation, λ = 800 nm, $\langle P \rangle \cong 2-4$ mW).

By applying the same procedure as the experiments run versus the bulk temperature on RhB decorated GNSs, the ESL measurements were performed on the fluorescence bursts (Figure 1B), and the temperature was deduced from the calibration curves reported in Figure 1A. The lifetime values measured on the background or the bursts display very similar percent changes as a function of the irradiation intensity. This observation suggests that dyes within the Debye distance from the outer particle layer, $\cong$15−30 nm,[31] feel a temperature similar to the bulk value when GNSs are irradiated by CW lasers at $I_{exc} \cong 4$ W/cm^{2}. The overall temperature increase obtained from the RhB excited state lifetime for gold nanorods and nanostars (λ = 800 nm, spot radius = 2 mm, CW excitation) is reported in Figure 2 as a function of the NIR laser intensity (0 W/cm^{2} $\leq I_{exc} \leq 7$ W/cm^{2}).

In order to study the temperature increase on magnetite nanoparticles we employed a gradient-index (GRIN) lens based endoscope to optically excite the RhB decorated paramagnetic nanoparticles (λ = 800 nm, 80 MHz rep. rate; 250 fs pulse width, beam waist $\cong$0.8 μm, average power $\langle P \rangle \cong 2-4$ mW). The GRIN lens coupled to the microscope objective allowed us

Figure 2. Temperature increase observed under CW irradiation at 800 nm as a function of the laser intensity. Panel A: temperature increase, ΔT, obtained from the excited state lifetime of the RhB in gold nanorods complexes (●) and from the direct thermograms (○). Panel B: temperature increase, ΔT, obtained from the RhB excited state lifetime in gold nanostars complexes (■) and from the direct thermograms (□). The excitation power of the pulsed laser that primes RhB fluorescence ranges from 2 to 4 mW, and the temperature was then corrected for the small increase due to the high peak excitation intensity according to Figure 5D.

to excite and observe the center of the RF solenoid, mounted 25 cm above the microscope focal plane (see "Endoscope for Magnetic–Optical Microscopy Measurements", in the SI) in such a way to reduce parasite currents in the metal parts of the microscope. The temperature increase measured from the ESL of RhB decorating magnetite nanoparticles under RF irradiation (ν = 168 kHz, B_{max} = 0.032 T) is reported in Figure 3 (open circles).
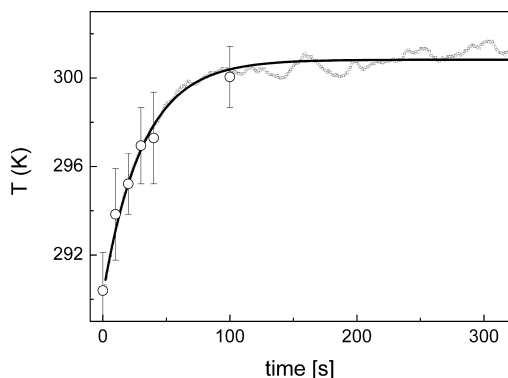
Figure 3. Thermogram of magnetite nanoparticles (C = 30 mg/mL) as a function of the RF irradiation time. The thermogram data were fit to the double exponential growth (eq 2, solid line). The values of temperature measured from the excited state lifetime of the RhB dye on the paramagnetic nanoparticles are reported as circles.

The optical method based on the measurement of the ESL of RhB$^+$ deposited on the surface of the nanoparticles allows us to monitor accurately the temperature in the close proximity ($\cong$20–30 nm as discussed below) of the nanoparticles and exploits therefore the spatial resolution of visible-NIR optical microscopy. Moreover the method devised here, which exploits the dependence of the RhB$^+$ ESL on the temperature, appears robust with respect to changes in the microenvironment. In fact although the absolute value of the RhB ESL changes in various environments, its slope, $(\partial \tau / \partial T)$, remains remarkably constant.

Temperature Increase from Irradiated Nanoparticles: Thermographic Measurements. The thermographic measurement (ThermaCAM SC 3000, FLIR System, see SI) reports the overall changes in temperature of the bulk sample and the information on the intrinsic thermal efficiency of the thermo-loaders (here the nanoparticles) are embedded in the details of the temperature increase kinetics.

The temperature increase of the gold nanoparticle suspensions under continuous irradiation with CW NIR laser (λ = 800 nm) can in fact be fit to two exponential components (Figure 4A,B) whose characteristic times are almost independent of the laser intensity in the range $2 \leq I_{exc} \leq 13$ W/cm^2:

$$T(t) = T_0 + \Delta T_1[1 - \exp(-t/\varphi_1)]$$
$$+ \Delta T_2[1 - \exp(-t/\varphi_2)] \quad (2)$$

As confirmed by numerical simulations below, the slower thermal growth with relaxation time φ_2 is due to the heat exchange with the environment and depends on the experimental setup: the suspension volume and its ratio to the excitation volume. The shorter growth time with characteristic time φ_1 is instead ascribed to the nanoparticle induced thermal load in the irradiation volume. Gold nanorods and nanostars display φ_2 values in the range 100–150 s (φ_2(GNRs)
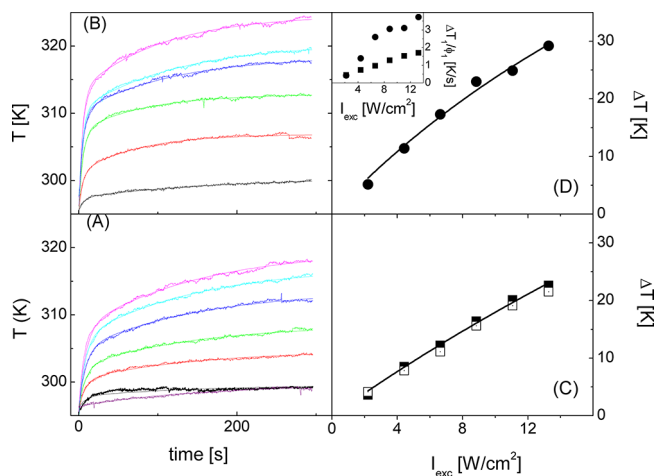
Figure 4. Thermograms of the irradiated suspensions. Panels A and B report the results from suspensions of GNR (panel A) and GNS (panel B). The temperature increase is shown as a function of time at different CW laser excitation intensities from the lowest (black symbols) to the largest (magenta symbols; I_{exc} = 2, 4.5, 6.7, 9, 11, 13.2 W/cm^2). In panel A, the purple line represents the CTAB alone at $\cong$3 W/cm^2. The continuous lines represent the global best fit of the data to eq 2. Panels C and D report the trend of the total temperature increase, $\Delta T_{tot} = \Delta T_1 + \Delta T_2$ (eq 2), as a function of the laser intensity for gold nanorods (panel C) and gold nanostars (panel D) suspensions. Full and empty squares in panel C refer to CW and pulsed (250 fs pulse width, 80 MHz repetition rate) excitation modes, respectively. The continuous lines represent the best fits of the data to the saturation curve: $\Delta T = \delta_T I_{exc}/(1 + I_{exc}/I_{sat})$. The best fit parameters are δ_T(GNRs) = 0.09 ± 0.006, I_{sat}(GNRs) = 43 ± 15 W/cm^2 and δ_T(GNSs) = 0.13 ± 0.01, I_{sat}(GNSs) = 19 ± 6 W/cm^2. The inset of panel D reports the ratios $\Delta T_1/\varphi_1$. The solid squares and circles refer to the gold nanorods and nanostars, respectively.

= 150 ± 25 s and φ_2(GNSs) =100 ± 22 s). The shorter growth time for gold nanorods, φ_1 = 8.5 ± 1 s, is approximately twice that measured for the gold nanostars, φ_1 = 4.8 ± 0.4 s.

The relation between the temperature increase and the NIR absorption of the gold nanoparticles is further confirmed by the linear dependence of $\Delta T_{tot} = \Delta T_1 + \Delta T_2$ on the NIR laser intensity (CW, λ = 800 nm) in the range $2 \leq I_{exc} \leq 13$ W/cm^2 (Figure 4C,D). The overall temperature increase found by the thermographic measurements (Figure 2, open symbols) is in very good agreement with the ESL results (Figure 2, filled symbols). A slight saturation, more pronounced for the gold nanostar suspensions, is visible above this value. The $\cong$30% difference in the values measured at $I_{exc} \cong$ 13 W/cm^2, ΔT_{tot}(GNRs) = 22.6 ± 0.2 K, and ΔT_{tot}(GNSs) = 29.2 ± 0.3 K, when normalized to the corresponding optical density (O.D.(λ = 800, GNSs) $\cong$ 1.4 and O.D.(λ = 800, GNRs) $\cong$ 0.5) corresponds to an increase of about 45 K and 21 K per optical density for GNRs and GNSs, respectively.

The gold nanoparticle suspension thermal load (Figure 4) under CW NIR irradiation is substantially confirmed when the NIR laser was switched to pulsed operation (250 fs pulses at 80 MHz repetition rate, 0.5 cm beam waist) as reported in Figure 4C. This indicates that the overall heat relaxation of the nanoparticles suspension is slower than the laser repetition time $\cong$ 12 ns (see also SI, Figure S9A).

Similar thermal loading experiments were run on magnetite nanoparticles irradiated by radio frequency (RF) radiation (ν = 168 kHz, B_{max} = 0.032 T). A drop of concentrated ($C_{MNP} \cong$ 30 mg/mL) magnetite nanoparticles was cast on a coverslip set at

the center of a 5.2 cm radius solenoid. The temperature of the suspension drop measured by the thermocamera raised exponentially to a plateau value $\Delta T \cong 10$ K above the basal temperature (kept at 291.1 ± 0.2 K by a chiller) as shown in Figure 3 (see "Description of the Thermoscan Movies of the Nanoparticle Suspensions" in the SI). Also in this case two exponential growth times (eq 2) could describe the data. A faster relaxation time, $\varphi_1 = 25 \pm 0.7$ s, corresponds to $\Delta T_1 = 11.5 \pm 0.5$ K, and a much slower one, $\varphi_2 = 430 \pm 130$ s, accounts for a minor $\Delta T_2 = 1.8 \pm 0.5$ K temperature increase. The overall temperature increase $\Delta T_{tot} = 13.3 \pm 0.4$ K is largely due to the Neel relaxation absorption of the nanoparticles.[8,22] Also in this case a very good agreement is found between the thermographic measurements of temperature and the ESL results (Figure 3). These data and the consideration drawn above indicate that the RhB lifetime provides us with a sensitive probe of the local temperature around gold or magnetite nanoparticles, irrespective of the excitation mode.

Moreover, gold nanoparticle suspensions, irradiated in the range 750−1000 nm, reach different equilibrium temperatures, $\Delta T_{tot}(I_{exc}) \cong 10-15$ °C, depending on the wavelength (Figure 1C,D, solid squares, see also movies in SI). The dependence of $\Delta T_{tot}(I_{exc})$ on the wavelength follows the extinction profile as expected due to the plasmonic resonances of the nanoparticles. This is particularly evident for the gold nanorod suspension (Figure 1D), for which minor scattering components are expected.[33] The nonvanishing temperature increase measured above 850 nm for gold nanorods is due to the NIR absorption of the CTAB surfactant alone, as reported in the SI (Figure S1). For the gold nanostars the maximum temperature increase, $\Delta T_{tot}(I_{exc})$, spans the range 10−15 °C in the whole 700−1000 nm interval. The reduced variability of $\Delta T_{tot}(I_{exc})$ for gold nanostars is probably due to a larger scattering contribution at 730 nm than at 970 nm as it is expected by analogy to complex gold nanostructures, such as for example silica gold nanospheres,[33] that present substantial scattering contribution to the extinction spectrum at lower energies. Nevertheless gold nanostars display thermal efficiency (ΔT_{tot}) similar to that of the gold nanorods and a wider range of IR wavelengths that can be exploited for hyperthermia compared to nanorods.

The gold nanoparticles appear to be more effective thermoloaders than the magnetic nanoparticles used here. In fact the volume fraction of the two types of suspensions differs substantially, being $\varphi \cong 10^{-5}$ and $\varphi \cong 10^{-3}$ for the gold and the magnetic nanoparticles, respectively. The heat capacity of the suspension irradiated by the NIR laser is therefore in any case indistinguishable from that of water. An exact measure of the specific absorption rate (SAR) should be performed under adiabatic conditions.[8,35] We provide here a lower limit by computing the SAR coefficient from the faster relaxation component of the thermogram kinetics (Figure 4D inset):

$$\text{SAR} = \frac{C}{m_{NP}} \frac{dT}{dt}\bigg|_{t=0} = \frac{C}{m_{NP}} \frac{\Delta T_1}{\varphi_1} \qquad (3)$$

The value computed on the gold nanorods and nanostars under $I_{exc} \cong 13$ W/cm^2 corresponds to $\cong 430 \pm 40$ kW/g and 190 ± 20 kW/g, respectively, that are almost 2 orders of magnitude larger than magnetite nanoparticles as reported from literature.[35] The SAR value of the magnetite particles investigated here corresponds in fact to SAR $\cong 0.2$ kW/g.

Spatial Inhomogeneity of Thermal Load around GNSs: Numerical Simulations and ESL Experiments. It

is relevant to study the origin of the two components in the heating kinetics and the extent of temperature inhomogeneity in space and time around the irradiated nanoparticles. Investigating the possibility to monitor space distribution of the temperature around a gold nanoparticle by ESL measurements is also relevant. To address these issues we have first simulated the heat released by gold nanoparticles under the irradiation of a Gaussian NIR laser beam. The temperature distribution was computed by numerically integrating the heat diffusion equation in radial coordinates and in 3D Cartesian coordinates as detailed in the SI ("Solution of the Heat Propagation Propagation around a Spherical Gold Nanoparticle"; the optical cross-section was computed on the nanoparticle shape by the ADDA code package).[36,34] Single nanoparticles were simulated either isolated or in contact with the bulk solution by assuming a constant or a time dependent temperature at the nanoparticle boundary (the radius of the available sphere per nanoparticle, $R_{bound} = ((4\pi/3)n)^{-1/3} \cong 1-3$ μm, where n is the number concentration of the nanoparticles): $T(R_{bound},t) = T_{bath} \cong 22$ °C or $T(R_{bound}) = T_{bath} + \Delta T_1 (1 - \exp(-t/\varphi_1))$ (see Figure 4A,B), respectively. Simulations were first performed under CW NIR irradiation (Figure 5A,B). On isolated nanoparticles we obtain a major exponential kinetics with a characteristic time $\varphi_1^{sim} \cong 25$ μs (Figure 5A, black symbols), and a second, minor and faster relaxation (see Table S1 for a list of the best fit parameters). The φ_1 time is determined by the thermal conductivity of the suspension (here taken as $\chi \cong \chi_{water} = 0.6$ W/m·K, due to the low volume fraction of the suspensions $\cong 10^{-3}$ to 10^{-5}). If χ is artificially lowered to $\chi = 0.3$ W/m·K, the relaxation time increases to $\varphi_1^{sim} \cong 50$ μs (Figure 5A, green symbols). The asymptotic temperature increase, ΔT, follows the laser excitation intensity ($\Delta T(1.6$ W/cm$^2) \cong 1$ K and $\Delta T(3.2$ W/cm$^2) \cong 2$ K; Figure 5A, blue and black symbols), and it depends on the efficiency of the thermal bath at R_{bound} ($\Delta T(R_{bound} = 3 \mu$m) $\cong 1$ K and $\Delta T(R_{bound} = 4.5 \mu$m) $\cong 2.2$ K; Figure 5A, black and red symbols). The effect of the Brownian movement of the nanoparticle through the excitation volume is that of smearing out the inhomogeneity (see "Solution of the Heat Propagation Propagation around a Spherical Gold Nanoparticle", Figure S9). The effect of the bulk solution on the single particle temperature was simulated by assuming $T(R_{bound}) = T_{bath} + \Delta T_1 (1 - \exp(-t/\varphi_1))$, with $\varphi_1 = 50$ ms (shorter than the experimental value $\varphi_1 \cong 100$ s, Figure 4A,B, for CPU time reasons) and $\Delta T_1 = 15$ °C. Also in this case the temperature increase at the nanoparticle surface occurs over times $\varphi_2^{sim} \cong 20-50$ μs (see Figure 5A inset, Table S3). However a slower relaxation time, $\varphi_1^{sim} \cong \varphi_1$, is also retrieved (see steep increase in T after 1 ms in Figure 5A inset) in agreement with the boundary condition. It seems therefore that the observed double relaxation increase of the temperature is related to the fast heat release from the nanoparticles and to the slow equilibration with the unirradiated volume. Real isothermal conditions can be simulated in the limit of increasing size of the simulation box and lead to further support to this hypothesis (see SI, "Solution of the Heat Propagation Propagation around a Spherical Gold Nanoparticle", Figure S9C).

Under CW NIR irradiation the spatial inhomogeneity of the temperature is limited to the first hundreds of microseconds of simulations (see Figure 5B): the maximum inhomogeneity is $\cong$ 9% after 300 μs and lowers to less than 2% after 2.5 ms. Even lower spatial inhomogeneity is expected in suspensions due to nanoparticle mobility (see Figure S9A). Spatial inhomogeneity
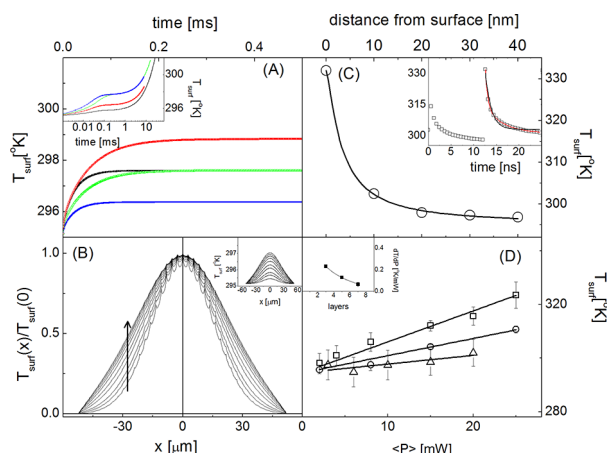
Figure 5. Simulation of the heat released by the nanoparticles in water suspensions. Panel A shows the result of the single particle simulation under isothermal boundary conditions, $T(R_{bound})$ = 295.15 K. The suspension heat conductivity was set to χ = 0.6 W/m·K (black, red, and blue symbols) and to χ = 0.3 W/m·K (green symbols). The excitation intensity was set to I_{exc} = 1.6 W/cm² (blue symbols) and 3.2 W/cm² (black, red, and green symbols). Boundary cell was changed from R_{bound} = 3 μm (black, green, blue symbols) to R_{bound} = 4.5 μm (red symbols). Inset shows the result of the single particle simulation under *experimental* boundary conditions, $T(R_{bound},t)$ = 295.15 + 15[1 − exp(−t/50)] (all times are in milliseconds). See also Table S3. Panels B, C: Simulation of the heat released by a set of immobile nanoparticles in water suspensions. Parameters: χ = 0.6 W/m·K, laser intensity I_{exc} = 3.2 W/cm²; layer thickness to D_l = 300 nm, one tenth of the interparticle distance (see text and SI for details). These simulations were run under isothermal boundary condition, $T(\pm L_{box})$ = 295.15 K. Panel B reports the spatial distribution of the temperature within the simulation box along a line passing through the center (L_{box} = 55 μm) in terms of absolute temperature (inset) and normalized temperature (panel B). The curves refer to increasing simulation times (from 0.3 to 4.4 ms) as indicated by the arrow. Panel C reports the simulated temperature kinetics and spatial distribution around a single GNR irradiated with a pulsed NIR laser (800 nm). The laser parameters are: T(period) = 12.5 ns, t_p = 400 fs (pulse width), <Power> = 1 mW, beam waist 1.5 μm. Main panel reports the temperature simulated at 1 ns from the laser pulse as a function of the distance from the nanoparticle. The solid line is the best fit hyperbolic decay[34] $T(r) \cong 295.15 + 36.8/(1 + (r/3.41)^{1.31})$, size in nanometers. Inset reports details of the temperature decay after a laser spot (squares) and best fit curves (single component, black line; decay time: 1.3 ± 0.1 ns; double component, red line; decay times: 0.5 ± 0.02 ns, 99% in intensity amplitude, and 4.1 ± 0.2 ns). Panel D reports ESL measurements on RHb decorated GNR with increasing number of polymeric layers: 3 (squares), 5 (circles), and 7 (triangles). The NIR laser was tuned at 800 nm, pulse width was 250 fs, repetition rate 80 MHz, beam waist $\cong$ 1.5 μm. Solid lines are the best global linear fit to the data. The corresponding slopes, in [K]/[mW], are reported in the inset. The solid decay corresponds to an exponential trend on the data.

depends also on the excitation mode.[34] For pulsed excitation (duty cycle $\cong 4 \times 10^4$, $I_{peak} \cong 1$ GW/cm², pulse width 200 fs) the surface of the nanoparticle can reach temperatures that are $\cong$ 10% higher than the boundary temperature (Figure 5C, S10) and relaxes in less than 1 ns (Figure 5C inset, black line). These fast temperature fluctuations die already at a distance $\cong$10 nm from the nanoparticle, with a spatial range much smaller than the CW irradiation case[34] (Figure 5C).

Based on this simulation output we have set up an experiment in which RhB decorated GNRs were observed while diffusing through the excitation volume and irradiated by high power 200 fs pulsed NIR laser (80 MHz repetition rate) tuned at 800 nm. Excitation power (2 mW $\leq \langle P \rangle \leq$ 50 mW) corresponds here to a wide range of peak intensity (1−70 GW/cm²), and the laser primes two-photon fluorescence emission from the dye and induces relevant temperature increase on the GNR surface that we monitor through the RhB excited state lifetime. GNRs were decorated for this purpose with 3, 5, or 7 polymeric layers in order to increase the spacing between the dye and the gold surface. The average lifetime measured on the fluorescence bursts (Figure S11), when converted to local temperature by means of eq 1, shows a definite increase in the temperature with the excitation power (Figure 5D), and it is sensitive to the distance from the gold surface (Figure 5D inset), decaying out over about 3−4 layers from the gold surface, that corresponds to 6.5−8.5 nm, not dissimilar from the simulated result (Figure 5C).

In conclusion, the possibility of measuring the temperature of the irradiated suspensions in situ by means of the excited state lifetime of RhB has been assessed on inorganic nanoparticles in which thermal loading was induced by electromagnetic irradiation. A comparison of the experiments performed under different excitation modes (pulsed/CW and collimated/focused) to numerical simulations indicates that the ELS method allows to test the temperature at less than 30 nm from irradiated nanoparticles, that is, less than the typical size of a cell. This would allow in principle to monitor temperature increase at the single particle level.

The sensitivity in the temperature measurements depends on the absolute number of photons that can be detected from a nanoparticle bound dye, which depends on the number of dyes, their photostability, and quantum yield and on the residence time of the nanoparticle in the observation volume. For a direct application of this ESL based thermometer to map temperature in the cells, similarly to what was recently reported on an acrylamide dye,[16] one should collect at least 2000 photons that, with the high brightness value shown by the RhB nanoconstructs developed here, should correspond to about 10−50 ms pixel residence time. A 100 × 100 pixels image in Fluorescence Lifetime Imaging mode[16] could then be acquired in 100−500 s. The robustness of the calibration procedure provided here suggests that the excited state lifetime measurements on RhB could be applied advantageously also for the characterization of the thermal efficiency (SAR) of widely varying types of nanoparticles irrespective of the excitation mechanism, thereby offering the possibility of comparison also in different environments.

Based on the optical and thermal measurements we are able to estimate the thermal efficiency of the two types of gold nanoparticles investigated here. The SAR, estimated in nonadiabatic conditions, is remarkably higher for the gold nanoparticles than for the super paramagenetic nanoparticles, and the gold nanostars have three times larger SAR than the gold nanorods. These data offer a promising background for the biomedical applications of gold nanostars as well as other nonspherical symmetric gold nanoparticles to hyperthermia, at least of superficial (<1 cm) diseases.[17]

■ ASSOCIATED CONTENT

Ⓢ Supporting Information

Materials and methods; optical extinction spectra; endoscopy for magnetic−optical microscopy measurements; simulations of the magnetic field; description of the thermoscan movies;

F

dx.doi.org/10.1021/nl400129v | Nano Lett. XXXX, XXX, XXX−XXX

solution of the heat propagation around a spherical gold nanoparticle; fitting of the simulated temperature kinetics; zeta potential characterization; Rhodamine B excited state lifetime as a function of pH; and measurements of the nanoconstructs. This material is available free of charge via the Internet at http://pubs.acs.org.

■ AUTHOR INFORMATION

Corresponding Author
*E-mail: giuseppe.chirico@mib.infn.it; psp@unipv.it.

Notes
The authors declare no competing financial interest.

■ ACKNOWLEDGMENTS

■ REFERENCES

(1) Wust, P.; Hildebrandt, B.; Sreenivasa, G.; Rau, B.; Gellermann, J.; Riess, H.; Felix, R.; Schlag, P. M. *Lancet Oncol.* **2002**, *3*, 487.

(2) Overgaard, J. *Int. J. Radiat. Oncol. Biol. Phys.* **1989**, *16*, 535.

(3) Westermann, A. M.; Jones, E. L.; Schem, B. C.; Van Der Steen-Banasik, E. M.; Koper, P.; Mella, O.; et al. *Cancer* **2005**, *104*, 763.

(4) Henle, K. J.; Dethlefsen, L. A. *Cancer Res.* **1978**, *38*, 1843.

(5) Hildebrandt, B.; Wust, P.; Ahlers, O.; Dieing, A.; Sreenivasa, G.; Kerner, T.; Felix, R.; Riess, H. *Crit. Rev. Oncol. Hematol.* **2002**, *43*, 33−56.

(6) Pattani, V. P.; Tunnell, J. W. *Lasers Surg. Med.* **2012**, *44*, 675.

(7) Chou, C.-H.; Chen, C.-D.; Wang, C. R. C. *J. Phys. Chem. B* **2005**, *109*, 11136.

(8) Hiroaki, M.; Balachandran, J. *Sci. Rep.* **2011**, *1*, 157.

(9) Truebel, H. K. F.; Maciejewski, P. K.; Farber, J. H.; Hyder, F. *J. Appl. Physiol.* **2003**, *94*, 1641.

(10) Comana, D.; Trubel, H. K.; Hydera, F. *NMR Biomed.* **2010**, *23*, 277.

(11) Albers, A. E.; Chan, E. M.; McBride, P. M.; Ajo-Franklin, C. M.; Cohen, B. E.; Helms, B. A. *J. Am. Chem. Soc.* **2012**, *134*, 9565.

(12) Shiraishi, Y.; Miyamoto, R.; Zhang, X.; Hirai, T. *Org. Lett.* **2007**, *9*, 3921.

(13) Zohar, O.; Ikeda, M.; Shinagawa, H.; Inoue, H.; Nakamura, H.; Elbaum, D.; Alkon, D. L.; Yoshioka, T. *Biophys. J.* **1998**, *74*, 82.

(14) Chen, Y. Y.; Wood, A. W. *Bioelectromagnetics* **2009**, *30*, 583.

(15) Donner, J. S.; Thompson, S. A.; Kreuzer, M. P.; Baffou, G.; Quidant, R. *Nano Lett.* **2012**, *12*, 2107.

(16) Okabe, K.; Inada, N.; Gota, C.; Harada, Y.; Funatsu, T.; Uchiyama, S. *Nat. Commun.* **2012**, *3*, 705.

(17) Hirsch, L. R.; Stafford, R. J.; Bankson, J. A.; Sershen, S. R.; Rivera, B.; Price, R. E.; Hazle, J. D.; Halas, N. J.; West, J. L. *Proc. Natl. Acad. Sci. U.S.A.* **2003**, *100*, 13549.

(18) Nikoobakht, B.; El-Sayed, M. A. *Chem. Mater.* **2003**, *15*, 1957.

(19) Pallavicini, P.; Chirico, G.; Collini, M.; Dacarro, G.; Dona, À.; D'Alfonso, L.; Falqui, A.; Diaz-Fernandez, Y.; Freddi, S.; Garofalo, B.; Genovese, A.; Sironi, L.; Taglietti, A. *Chem. Commun.* **2011**, *47*, 1315.

(20) Sironi, L.; Freddi, S.; Caccia, M.; Pozzi, P.; Rossetti, L.; Pallavicini, P.; Donà, A.; Cabrini, E.; Gualtieri, M.; Rivolta, I; Panariti, A.; D'Alfonso, L.; Collini, M.; Chirico, G. *J. Phys. Chem. C* **2012**, *116*, 18407.

(21) Casu, A.; Cabrini, E.; Dona, A.; Falqui, A.; Diaz-Fernandez, Y.; Milanese, C.; Taglietti, A.; Pallavicini, P. *Chem.—Eur. J.* **2012**, *18*, 9381.

(22) Baldi, G.; Lorenzi, G.; Ravagli, C. *Process. Appl. Ceram.* **2009**, *3*, 103.

(23) Baldi, G.; Bonacchi, D.; Innocenti, C.; Lorenzi, G.; Sangregorio, C. *J. Magn. Magn. Mater.* **2007**, *311*, 10.

(24) Kitamura, N.; Hosoda, Y.; Iwasaki, C.; Ueno, K.; Kim, H.-B. *Langmuir* **2003**, *19*, 8484.

(25) Mchedlov-Petrossyan, N. O.; Vodolazkaya, N. A.; Doroshenko, A. O. *J. Fluor.* **2003**, *13*, 235.

(26) Dulkeith, E.; Morteani, A. C.; Niedereichholz, T.; Klar, T. A.; Feldmann, J.; Levi, S. A.; van Veggel, F. C. J. M.; Reinhoudt, D. N.; Moeller, M.; Gittins, D. I. *Phys. Rev. Lett.* **2002**, *89*, 203002.

(27) Freddi, S.; D'Alfonso, L.; Collini, M.; Chirico, G. *J. Phys. Chem. C* **2009**, *113*, 2722.

(28) El Haitami, A. E.; Martel, D.; Ball, V.; Nguyen, H. C.; Gonthier, E.; Labbé, P.; Voegel, J.-C.; Schaaf, P.; Senger, B.; Boulmedais, F. *Langmuir* **2009**, *25*, 2282.

(29) Cavallaro, G.; Giammona, G.; Pasotti, L.; Pallavicini, P. *Chem.—Eur. J.* **2001**, *17*, 10574.

(30) Sironi, L.; Freddi, S.; D'Alfonso, L.; Collini, M.; Gorletta, T.; Soddu, S.; Chirico, G. *J. Biomed. Nanotechnol.* **2009**, *5*, 683.

(31) Manning, G. S. *Phys. Chem.* **1996**, *100*, 909−922.

(32) Chen, H.; Shao, L.; Ming, T.; Sun, Z.; Zhao, C.; Yang, B.; Wang, J. *Small* **2010**, *6*, 2272.

(33) Prashant, K. J.; Lee, K. S.; El-Sayed, I. H.; El-Sayed, M. A. *J. Phys. Chem. B* **2006**, *110*, 7238.

(34) Baffou1, G.; Quidant, R. *Laser Photonics Rev.* **2013**, *7*, 171−187.

(35) Huang, S.; Wang, S.-Y.; Gupta, A.; Borca-Tasciuc, D.-A.; Salon, S. *J. Meas. Sci. Technol.* **2012**, *23*, 035701.

(36) Yurkin, M. A.; Hoekstra, A. G. *J. Quant. Spectrosc. Radiat.* **2011**, *112*, 2234.